Chinese Chemical Letters 34 (2023) 108471

Contents lists available at ScienceDirect

Chinese Chemical Letters

journal homepage: www.elsevier.com/locate/cclet

Inspired by nature: Self-fractal cobalt sulfate composite electrode for sodium ion storage

Man Zhang[a], Xiaoxu Liu[a,*], Jiangdong Gu[a,*], Hui Wang[b], Hui Liu[a], Zexiang Shen[b]

[a] Shaanxi Key Laboratory of Green Preparation and Functionalization for Inorganic Materials, School of Material Science and Engineering, Shaanxi University of Science and Technology, Xi'an 710021, China
[b] Division of Physics and Applied Physics School of Physical and Mathematical Sciences, Nanyang Technological University, Singapore 637371, Singapore

ARTICLE INFO

Article history:
Received 4 February 2023
Revised 10 March 2023
Accepted 18 April 2023
Available online 21 April 2023

Keywords:
Fractal structure
Cobalt sulfate
SAXS
Sodium-ion battery
Anode material

ABSTRACT

Generally, the metal sulfide itself has poor conductivity, and the volume expansion occurs when it is converted with sodium, which will destroy the integrity of the electrode structure, resulting in poor cycle performance and rate performance. To solve the problems of low initial coulombic efficiency (ICE) and volume expansion of metal compounds used as anodes in sodium-ion batteries (SIBs). Inspired by nature, the $CoSO_4$/hard carbon/graphene (CHG) fractal structure electrode was designed. Self-fractal structures with electron/ion transport channels and high strain tolerance proved to be an effective strategy to overcome these challenges. The fractal dimension (D) is measured by synchronous Small Angle X-ray scattering, and the D remains stable during charging and discharging. The fractal CHG also showed excellent electrochemical performance, especially 97.4% ICE. Theoretical calculation shows that self-fractal CHG can promote the formation of a thin solid electrolyte interface (SEI). Synchrotron radiation absorption spectrum proved the reaction mechanism of CHG. This study not only proves that cobalt sulfate is a feasible strategy for developing high-performance SIBs anodes but also provides an advanced method for measuring the fractal dimension of energy storage electrode materials.

Lithium-ion batteries (LIBs) are currently the main commercial energy storage devices. Although profound progress in LIBs systems has been made in recent years, restricted lithium resources and high costs have prompted researchers to focus on developing alternative rechargeable batteries [1,2]. Currently, sodium-ion batteries (SIBs) are considered ideal candidates for efficient and economical energy storage technology due to their low cost and abundant resources [3]. Researchers have been working hard to find suitable anode materials for sodium energy storage. In recent years, metal compounds, *e.g.*, oxides [4], phosphides [5,6] and sulfides [7], have aroused much interest owing to their unique physical properties and promising applications in the field of energy storage/energy conversion application [8,9]. However, the above-mentioned metal compound materials generally have problems such as complex synthesis processes, high costs, and poor long-term cycle performance in applications [10]. As a potential cathode material for rechargeable batteries, sulfate has the characteristics of green, low price, low toxicity, and wide reserves [11]. However, sulfate lacks in-depth research in anode materials. Therefore, it is of great significance to study environmentally friendly and cost-effective cobalt sulfate electrode materials. In general, electrode failure is almost inevitable when using inorganic compounds as anode materials during charging/discharging due to large volume expansion [12]. To curb the volume change of electrode materials, provide high conductivity and great volume change adaptability, rational structural design [13], or introduction of advanced carbon materials [14] are widely used strategies. Therefore, using graphene as a substrate and designing a fractal structure under a controllable path would be one of the potential ways to improve the sodium storage performance of cobalt sulfate.

The fractal structure can be seen everywhere in nature and has a unique structure that can adapt to the natural environment, which is worthy of our reference. For example, plants in nature capture sunlight layer by layer through multi-level fractal structures composed of branches and leaves, making full use of energy. Therefore, the electrode with a bionic fractal structure has the advantages of a large specific surface area and micro-nano multilayer structure and has a good application prospect in the field of energy storage devices [15]. In recent years, the design and development of layered materials inspired by fractal materials in nature have achieved positive results [16]. For example, researchers have found that electrode materials designed with fractal structures can

* Corresponding authors.
E-mail addresses: xiaoxuliu@sust.edu.cn (X. Liu), 44842292@qq.com (J. Gu).

https://doi.org/10.1016/j.cclet.2023.108471
1001-8417/

be used for capacitors to achieve high specific capacitance and cycle stability [17]. This is attributed to the fact that the fractal structure has sufficient electrode/electrolyte contact, and high strain tolerance capability. It effectively increases the reactive active site and prevents mechanical aggregation and structural collapse [18]. It is important to note that dimension is an important parameter for geometry. The dimension of the fractal structure is between one dimension and two dimensions or between two dimensions and three dimensions, showing a non-integer form of dimension. For fractal structures, the larger the dimension, the more complex it is [19]. Therefore, knowing the fractal dimension of the structure helps to design suitable electrode materials. However, the application of fractal structure materials in battery energy storage systems is less, and there is a lack of suitable testing methods to measure the fractal dimension [20]. So far, the synchrotron radiation small angle X-ray scattering (SAXS) method is widely used to study fractal structures of irregular objects and obtain quantitative structural parameters. If the system has a fractal structure, its structural characteristics must be reflected in the scattering intensity, and the fractal dimension can be easily obtained from the slope of the measured intensity as a function of the wave vector in the log-log coordinate system [21]. Its fractal dimension can be divided into mass fractals (D_m) and surface fractals (D_s). The D_m reflects the aggregation state and density of particles and groups. The smaller is D_m, the sparser the sample structure. D_s indicates the irregularity or roughness of the nanoparticle fractal, while the larger D_s indicates the rougher or higher irregularity of the sample surface.

Although the theoretical quantitative description of the fractal structure by SAXS has existed for a long time, few studies are using SAXS to quantitatively analyze the fractal structure of electrode materials for battery energy storage. Herein, inspired by fractal snowflakes in nature, we designed and synthesized a flexible freestanding $CoSO_4$/hard carbon/graphene (CHG) material with a self-fractal structure. The fractal dimension of the composite electrode was quantitatively measured by synchrotron radiation SAXS, and its special hierarchical structure was quantitatively described. The unique flake fractal structure endows the CHG electrode with excellent electron and ion conductivity as well as structural stability, to effectively promote the rate performance and cycle performance. The key of 97.44% initial coulombic efficiency (ICE) in the CHG electrode was explored by X-ray photoelectron spectroscopy (XPS) and theoretical calculation. In addition, the sodium storage mechanism for the CHG electrode was studied by *ex-situ* X-ray absorption fine structure (XAFS), XPS, and transmission electron microscopy (TEM). This study provides a technical model and theoretical guidance for the design of self-fractal anode materials with excellent sodium storage performance.

The self-fractal CHG electrode material is a sheet-like layered three-level structure, in which the primary structure is a centimeter-scale three-dimensional sheet-like graphene framework (GF); the secondary structure is a micron-scale $CoSO_4$/hard carbon (CH) carbon grown on the GF composite lamellar structure; the tertiary structure is nanosheets of hard carbon and $CoSO_4$ that make up the CH composite lamellae. This macroscopic to microscopic self-similar structure is similar to that of natural self-fractal snowflakes (Figs. 1a–d, Figs. S1 and S2 in Supporting information)). In comparison, CH is fractured and crushed without a graphene skeleton during preparation, presenting an irregular morphology (Fig. S3 in Supporting information). X-ray diffraction (XRD) indicates that obtained CHG composite is well indexed to a typical pyrite-type $CoSO_4$ (JCPDS card No. 54-1124) (Fig. S4 in Supporting information). CHG has a higher I_D/I_G ratio in the Raman spectrum than graphene, indicating more hard carbon with defects (Fig. S5 in Supporting information) [22]. In order to quantitatively describe the fractal dimension D of the fractal structure, SAXS was

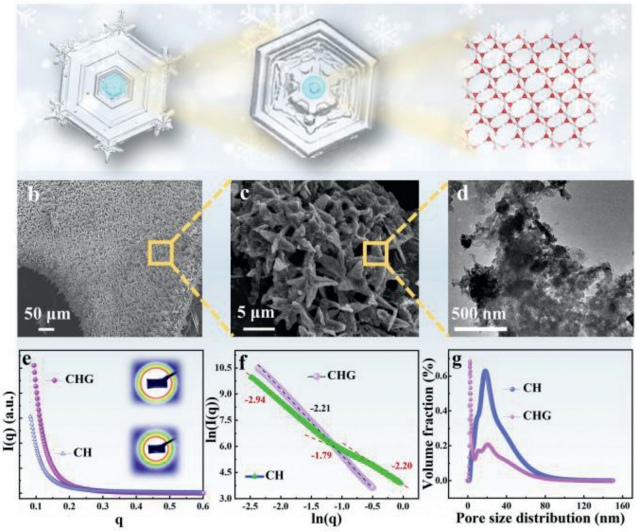

Fig. 1. Fractal structure of CHG. (a) Images of snowflakes from a macroscopic to crystalline structure. (b, c) Scanning electron microscope (SEM) image of CHG. (d) TEM image of CHG. (e) SAXS curves (inset: SAXS images). (f) Linear fitting of ln(q)-ln(q) scattering data and (g) pore size distribution images of CHG and CH, respectively.

conducted, and the test results are shown in Figs. 1e–g. According to previous reports, the fractal dimension of the composite system can be calculated using the data in Fig. 1e [23–25]. The SAXS patterns are fitted with the Fractal model after taking the logarithm of its horizontal and vertical coordinates, whose results are shown in Fig. 1f. It can be seen that CHG has good linearity and only one fractal dimension, 2.21, indicating that it has a good self-fractal structure. In comparison, CH has multiple fractal dimensions of 1.79, 2.20 and 2.94, indicating no obvious self-fractal characteristics. In addition, the pore size distribution in the self-fractal system can be calculated by using the step-by-step cutting method (Fig. 1g) [26]. The results show that CHG has a single pore size distribution of 20 nm, while CHG samples have an obvious multi-scale pore distribution from several nanometers to tens of nanometers. These results indicate that multiscale nanostructures exist in CHG samples, which will be further confirmed by TEM.

The morphology and microstructure of the CHG were further investigated by TEM (Figs. 2a–c). As shown in Fig. 2b and Fig. S6 (Supporting information), $CoSO_4$ nanosheets and carbon nanosheets can be observed in TEM images. High-resolution TEM (HRTEM) provides further insight into the detailed structure. Clear lattice fringes with an interplanar spacing of 0.25 nm can be observed in Fig. 2c, which can be assigned to the $(00\bar{2})$ planes of $CoSO_4$. The corresponding selected area electron diffraction (SAED) pattern of this CHG is shown in Fig. 2d. A bright diffraction ring in the SAED image is indexed to graphene phases, agreeing well with the XRD results. The structural evolution process of fractal structure CHG is shown in Fig. 2a, combined with SEM and TEM analysis. The scanning transmission electron microscopy (STEM) of CHG can observe that the sample is composed of a large number of nanosheets stacked up. Corresponding energy-dispersive X-ray spectroscopy (EDS) element mappings (Fig. 2e) shows homogenous distributions of Co, S, C, N and O elements in the sample, confirming the $CoSO_4$ nanosheet wrapped by carbon nanoflakes. The above results again indicate that the structure of self-fractal CHG composites is as follows: hard carbon and $CoSO_4$ nanosheets are stacked to form CH microscale sheets, and CH arrays are grown on millimeters scale GF. In addition, thermogravimetric (TG) analysis showed that the content of $CoSO_4$ and hard carbon/graphene

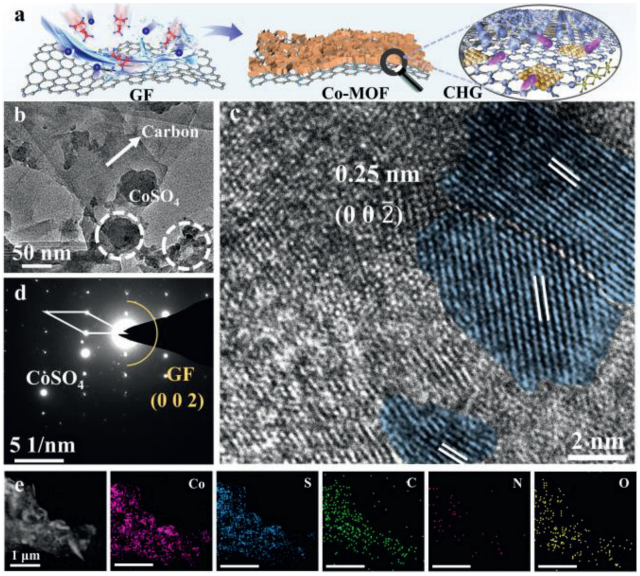

Fig. 2. Microstructure of fractal CHG. (a) Schematic of CHG structure evolution. (b) TEM and (c) HRTEM images of the CHG sample. (d) Corresponding SAED pattern of CHG. (e) STEM image of the CHG sample and corresponding EDS mappings of Co, S, C, N and O elements.

in CHG was 18.5% and 81.5%, respectively. (Fig. S7 in Supporting information) [27].

The electrochemical properties of CHG, CH, and GF were evaluated in SIBs, respectively. The charge/discharge capacities of CHG are 357.5 and 366.9 mAh/g with a high ICE of 97.4% at a current density of 0.05 A/g. For the following two cycles, the discharge/charge curves are highly overlapped with coulombic efficiency immediately increasing to more than 99%, indicating outstanding reversibility (Fig. 3a and Fig. S8 in Supporting information). It is worth noting that the discharge curve of the first cycle of CHG is very different compared to other cycles, which can be attributed to the intrinsic properties of the CHG electrode and the formation of a solid-electrolyte interface (SEI). In subsequent cycles, the discharge curve becomes stable due to polarization and activation of the electrode material. As shown in Fig. 3b, it delivers capacities of 345.5, 276.3, 249.6, 202.8 and 146.1 mAh/g at current densities of 0.05, 0.1, 0.2, 0.5 and 1.0 A/g, respectively. The discharge capacity reverts to 255.4 mAh/g when the current density is restored to 0.05 A/g. Moreover, CHG maintains a discharge capacity of 228.9 mAh/g after 50 cycles at 0.1 A/g (Fig. 3c). According to the electrochemical performance, it can be found that $CoSO_4$ greatly increases the specific capacity of CHG (Fig. S9 in Supporting information), and the unique fractal structure promotes the migration of ions/electrons and improves diffusion kinetics. In addition, the hard carbon physically confines the cobalt sulfate decomposition products, thereby improving the reaction reversibility. Moreover, the gap between the different layers of the fractal structure can provide enough space to overcome the volume expansion during the sodiation/desodiation process and ensure the stability of the electrode material. In contrast, the structure of CH collapses, thus CH provides limited channels for ion/electron transport, and cannot alleviate the volume expansion during the charging and discharging process, which ultimately leads to electrode failure. Therefore, when CH is used as the anode material of SIBs, the ICE of CH is only 55.88%, the rate performance is poor (Fig. S10 in Supporting information), and the capacity continues to decrease during the cycle. The capacity was reduced to 32 mAh/g after 100 cycles at a current density of 0.1 A/g (Fig. 3c). In addition, the ICE, voltage platform, and rate performance of CHG anodes outperform other reported sulfides (Table S1 in Supporting information). And CHG also exhibits a sufficiently high ICE and capacity compared to similar free-standing electrodes (Table S2 in

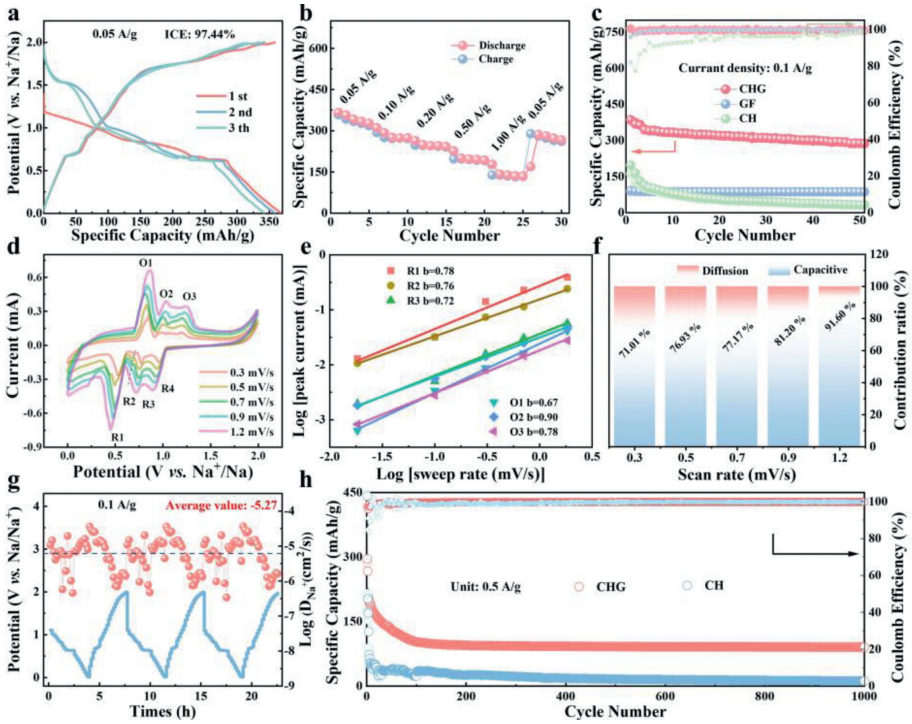

Fig. 3. Electrochemical performance. (a) Charge-discharge curves of CHG at 0.05 A/g. (b) Rate performance of the CHG electrodes. (c) Cycling stability and coulombic efficiency of CHG, CH and GF at 0.1 A/g. (d) CV curves of CHG at different scan rates. (e) Corresponding log(*i*) *vs.* log(*v*) plots at different redox states of the as-prepared CHG electrode. (f) Bar chart showing the percent of pseudocapacitive contribution of CHG at different scan rates. (g) Na^+ diffusion of CHG at a state of charge-discharge. (h) Cycling stability and Coulombic efficiency of CHG and CH at 0.5 A/g.

Supporting information). To further study the reaction kinetics of the CHG, the cyclic voltammetry (CV) at different scan rates was carried on (Figs. 3d–f, Figs. S11 and S12 in Supporting information) [28]. As shown in Fig. 3d, all peak currents (i) upgrade as the scan rates (v) ascend. Among them, the presence of a cathode peak at R1 (0.98 V) corresponds to the formation of Co and Na_2S in an irreversible reaction (Eqs. S1-S4 in Supporting information). The redox peaks at 2.0 V and 0 V correspond to the reversible reaction process of $NaCoS_2$ (Eq. S5 in Supporting information). In addition, the three main cathode peaks at R1 (0.56 V), R2 (0.70 V) and R3 (0.78 V), and the three main anode peaks at O1 (0.85 V), O2 (1.05 V), and O3 (1.19 V) may be reversible intercalation reactions of substrate GF (Fig. S11). Fig. 3e presents log(i) *vs.* log(v) plots of the six redox peaks, and the slope of the fitted line is represented by b. When $b = 0.5$, the electrochemical reaction is controlled by ionic diffusion, and when $b = 1$, pseudocapacitive behaviors are dominant. The calculated b values are all between 0.5 and 1.0, indicating that the Na^+ storage process of the CHG electrode is influenced by both diffusion control and pseudocapacitance control. In addition, the contribution ratio of pseudocapacitance increases with the increase in scanning rate (Fig. 3f). Moreover, Compared with CH, fractal CHG has a higher pseudocapacitance contribution and even reached 91.6% at the scanning rate of 1.2 mV/s. This predominant pseudocapacitive behavior would account for the excellent rate performance of CHG to a certain degree. The galvanostatic intermittent titration technique (GITT) was performed to investigate the migration of Na^+ in CHG, and the distinct two pairs of potential platforms are probed using GITT curves, which once again confirmed the multiphase reaction of sodiation/desodiation for the CHG electrode (Fig. 3g and Fig. S13 in Supporting information) [29]. Mostly, CHG possesses higher D_{Na^+} than CH, which can be attributed to the larger pseudocapacitance contributions and the unique fractal structure as an ion reservoir to create a fast channel for Na^+. For the discharge process, the D_{Na^+} value decreases with the increase of the Na^+ contents. Due to the formation of a multiphase compound *via* a stepwise conversion reaction, the Na^+ diffusion reaches a minimum at corresponding discharge voltage platform regions of 0.8 and 0.6 V (Eqs. S1-S4). After a complete transition from a mixed metal oxide phase to Co metals accompanied by the generation of Na_2S, the ion diffusion coefficient reaches the maximum (Eq. S5). Correspondingly, the extraction behaviors, redox reactions, and structure rearrangement occur in the charging process due to reductive D_{Na^+} values. The electrochemical impedance spectrum (EIS) was further used to study the reaction kinetics of electrode materials (Fig. S14 and Table S3 in Supporting information). The CHG electrode has a small charge transfer resistance and a large σ value (181.91) [1]. These results demonstrate excellent ion transport for the CHG electrode. Thus, CHG has a long cycle life with a reversible capacity of 110 mAh/g even after 1000 cycles at 0.5 A/g (Fig. 3h). It can be seen that CHG has excellent electrochemical performance. Most notably, the ICE is important in battery research as a quantifiable indicator of battery life, energy density, and rate performance [30,31]. Compared with other sulfides, GHC shows higher ICE. To explore the reason why CHG has such high ICE, XPS spectrum and density functional theory (DFT) calculation are applied in the next paragraph.

Ex-situ SAXS, XPS and DFT calculations were used to investigate the cause of high ICE in the composites. *Ex-situ* SAXS proved that CHG maintained its original fractal structure after the initial charge and discharge, and the stable structure was conducive to the ion/electron insertion/extraction (Fig. S15 in Supporting information). XPS elemental analysis after different Ar^+ sputtering times shows that CF_x greatly decreases with increasing sputtering time and NaF dominates F 1s spectra after sputtering 20 s, indicating that the SEI is rich in inorganic components (Fig. 4a and Fig. S16 in Supporting information) [32]. The absence of Na_2SO_3 in S 2p

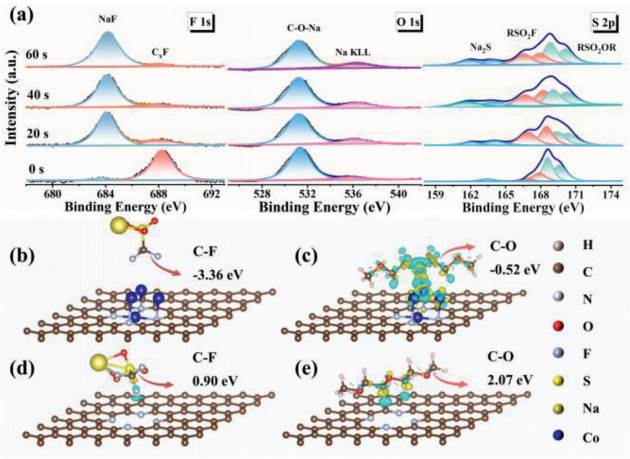

Fig. 4. The catalytic mechanism of CHG. (a) High resolution XPS spectrum of CHG, with sputtering time for 0, 20, 40 and 60 s, respectively. Differential charge densities of (b) $NaSO_3CF_3$–CHG, (c) DIGLYME-CHG, (d) $NaSO_3CF_3$–CH, (e) DIGLYME-CH. Yellow and cyan isosurfaces show the electron gain and electron loss, respectively.

spectrum further verified that NaF is the main product of the inorganic layer of SEI [33]. In addition, F-C(sp^2) (688.84 eV) almost disappears in F 1s spectrum when discharging to 0.01 V. It is inferred that, on one hand, the larger CH sheets at the micron scale will reduce the contact between the active material and the electrolyte; on the other hand, the pores between the fractal structures can enhance the infiltration of the electrolyte. Therefore, the continuously generated Co atoms/clusters catalyze the sufficient decomposition of a smaller amount of the electrolyte, which improves the coulombic efficiency.

In order to further investigate the catalytic and adsorption of electrolytes by CHG, DFT calculations were used. In the structure of $NaSO_3CF_3$ on CHG, the bond dissociation energy of the C-F bond (−3.36 eV) is lower than that of the C–S bond (0.90 eV), suggesting C-F is more liable after the first discharge. This is attributed to a large number of electrochemically active sites in the fractal structure, which can generate more Co atoms/clusters at the first discharge, thus reducing the dissociation energy of the C-F bond and making it easier for F^- to connect with Na^+ to form NaF. Moreover, as the F atom decreases, the dissociation energy of the C-F bond decreases (Figs. 4b and d, Table S4 in Supporting information). Besides, the adsorption energy of sodium sulfonate on CHG is more negative, indicating that the composite material can adsorb electrolytes more stably (Fig. S17 and Table S4 in Supporting information). Similarly, CHG also shows a better catalytic effect and lower adsorption energy for DIGLYME (Figs. 4c and e, Fig. S18 and Table S4 in Supporting information). The charge distribution of CHG is also revealed by the charge density differences. The accumulated charge at the interface of CHG confirms the enhanced charge transfer between DIGLYME and Co atoms/clusters, which is expected to accelerate the reaction/decomposition of electrolytes during the discharge/charge process. The above analysis shows that the aggregation of discharge products is suppressed due to the good wettability of the self-fractal structure, the number of electrochemically active sites at the "active material/electrolyte" interface, as well as the ultra-small nanocluster size, and efficient bonding rivets. It is beneficial to CHG catalytic electrolyte separation, thus CHG electrode material can show higher coulombic efficiency.

The *ex-situ* XPS (Fig. 5a and Fig. S19 in Supporting information) and *ex-situ* TEM (Figs. 5b–d and Fig. S20 in Supporting information) were used to confirm the reaction products and understand the structural changes of CHG upon cycling. Fig. 5a shows the XPS patterns of CHG at different states in Na half cells. As seen in the

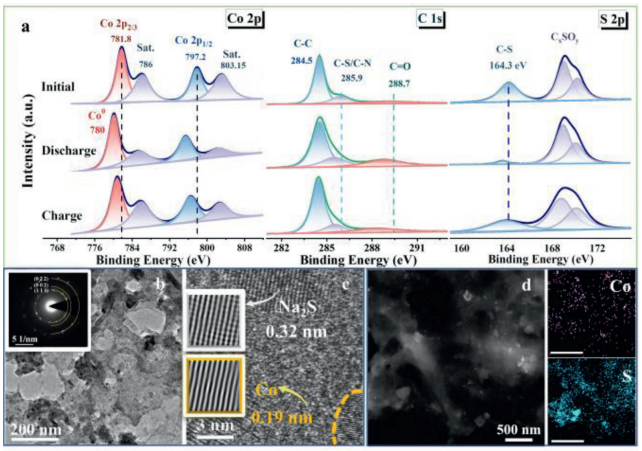

Fig. 5. The reaction mechanism of CHG. (a) *Ex-situ* high-resolution XPS spectrum of CHG. (b) TEM, (c) HRTEM and (d) TEM-EDS mapping results for selected elements of CHG discharged to 0.01 V.

Co 2p spectra, compared with the original electrode, the peaks of Co $2p_{3/2}$ and Co $2p_{1/2}$ were red-shifted during the discharge process and blue-shifted during the charging process, proving the occurrence of a reversible reaction. After full discharge, the Co^0 peak appears at 780.0 eV, and compound $NaCoS_2$ is generated after charging, due to an incomplete transformation reaction [34]. In the C 1s spectra, the C-S/C–N (285.9 eV) and C=O (288.7 eV) peak red-shifted in both the discharge and charge processes compared to the pristine electrode, evidencing the irreversibly sodiation of S and O in CHG after the first charge [35]. Multiple peaks can be observed due to different S species in the composite. Two evident peaks at 167.0 and 170.3 eV are attributed to C_xSO_y $2p_{3/2}$ and $2p_{1/2}$, and the C-S peak (164.3 eV) moved during the reaction, indicating that S in CHG was involved in the redox reaction. Meanwhile, black dots appear on the TEM image after the discharge. The HRTEM image at 0.01 V exhibits two sets of lattice fringes of 0.19 and 0.32 nm, corresponding to the (111) plane of metallic Co and (200) plane of Na_2S (Fig. 5c). In addition, In TEM dark field, bright spots were also observed, indicating the formation of metal Co (Fig. 5d). When the electrode was charged to 2 V, the lattice fringes of crystalline $NaCoS_2$ can be observed in the TEM image at 2 V (Fig. S20). This proves the reaction mechanism of fractal CHG electrode materials.

To gain further insights into the conversion reaction of CHG, X-ray absorption fine structure, including X-ray absorption near-edge structure (XANES) and extended X-ray absorption fine structure (EXAFS), was used to scrutinize the evolution of the coordination environment and the chemical state upon cycling [36]. In Fig. 6a and Fig. S21a (Supporting information), the different cut-off voltages of the XAFS spectra at the Co K-edge are compared. As can be seen, the XANES spectra of the pristine CHG display a small pre-edge peak at around 7110 eV, which suggests octahedral coordination of Co by O [37]. The Co K-edge spectrum shifts to lower energy as the potential decreases to 0.01 V, which indicates that the Co^{2+} is reduced to a lower valence during the discharge process. During the charging process, the Co K-edge shift exhibits the inverse trend, indicating that a partially reversible reaction has taken place [38]. Fig. 6b and Fig. S21b (Supporting information) present the Fourier transformed EXAFS spectra of the Co K-edge at corresponding discharge/charge states. The peak appearing at around 2.08 Å is attributed to the Co–O interaction in the CHG composite. The intensity of the Co–O bond decreases and the width increases with the discharging depth, which may be because Na^+ ions are gradually inserted into the $CoSO_4$ to form small domain sizes of the Co metal and make the local structure disordered, which is manifested in two new peaks in the EXAFS spectrum. During charging, cobalt disappears and the coordination environment of CHG changes to the initial sample. However, since the conversion reaction of the electrode is not completely reversible, and the new compound $NaCoS_2$ is used as the raw material for the following reaction, a new peak appears at the end of charging, which represents the coordination environment of $NaCoS_2$. The bond length and coordination number information are obtained by fitting EXAFS spectrum (Figs. 6c and d, Fig. S21c and Table S5 in Supporting information). When the discharge was completed, the bond length of Co-O increased significantly while the coordination number decreased, indicating that the O coordination of Co atom was gradually converted to Co–Co coordination. During the charging process, the coordination environment of Co atoms did not return to the initial coordination state of O atoms, but a new Co–S coordination environment appeared, representing the formation of $NaCoS_2$, and the results are consistent with EXAFS spectra. Wavelet transformed (WT) EXAFS analysis is also involved as a potent method to distinguish the contribution of each pathway for providing both R-space and k-space resolution at the same time

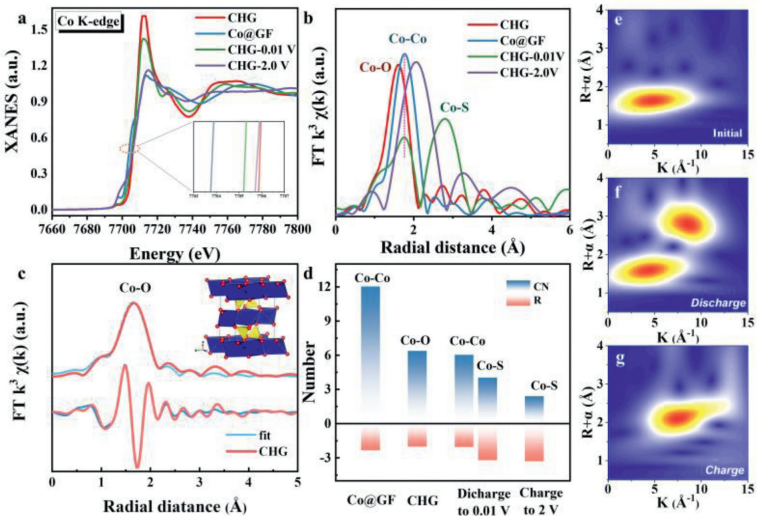

Fig. 6. The reaction mechanism of CHG. (a) Co K-edge XANES spectra. (b) Fourier transformed k^3-weighted $\chi(k)$ function of the EXAFS spectra collected at the Co K-edge. (c) Fourier transformed k^3-weighted $\chi(k)$ function of the EXAFS spectra collected at the Co K-edge after fitting. (d) bar graph of EXAFS data after fitting. (e–g) the wavelet transforms of EXAFS signals of CHG at different discharge/charge states.

(Figs. 6e–g and Fig. S21d in Supporting information) [36]. From the full discharge state, the Co–O bond disappears and the scattering path of Co–Co and Co–S appears, corresponding to the conversion reaction. In the charging process, only Co–S exists, indicating that part of the irreversible reaction occurs. This is consistent with the results of *ex-situ* XPS and TEM, which further proves the reaction process.

In summary, we developed a self-fractal structure CHG as an electrode material of SIBs. Similar to fractal structures in nature, CHG has good porosity and structural stability. The fractal dimension of the material was quantitatively described by SAXS, which was 2.21. Due to the excellent performance of the fractal junction, the CHG electrode shows excellent rate performance and good cycle stability due to the fast speed of electron/ion transport in the repeated charge and discharge process. DFT calculations and XPS spectra show that due to the good wettability of the fractal structure and numerous active sites, even though the large-sized CHG electrode has few contact interfaces with the electrolyte, it can be fully decomposed to reduce electrolyte consumption, resulting in excellent ICE performance. *Ex-situ* XPS, TEM and XAFS have confirmed the reaction mechanism: cobalt metal is produced in the first discharge. The initial discharge produces cobalt metal and $NaCoS_2$, which are converted during the subsequent charge and discharge process. This study provides a new method for quantifying the hierarchical structure information of electrodes with self-fractal characteristics. The mechanism of sodium storage for cobalt sulfate composite electrodes is proposed, which provides technical materials and theoretical guidance for the anode design for sodium storage with high ICE.

Declaration of competing interest

The authors declare that they have no known competing financial interests or personal relationships that could have appeared to influence the work reported in this paper.

Acknowledgments

This work was supported by Beijing Synchrotron Radiation 1W2A Work Station and 4B9A Work Station in China and was financially supported by National Natural Science Foundation of China (No. 52250710161).

Supplementary materials

Supplementary material associated with this article can be found, in the online version, at doi:10.1016/j.cclet.2023.108471.

References

[1] J. Wu, S. Liu, Y. Rehman, et al., Adv. Funct. Mater. 31 (2021) 2010832.
[2] C. Guo, J. Yang, Z. Cui, et al., J. Energy Chem. 65 (2022) 514–523.
[3] X. Liu, T. Wang, T. Zhang, et al., Adv. Energy Mater. 12 (2022) 2202388.
[4] C. Hao, T. Gao, A. Yuan, et al., Chin. Chem. Lett. 32 (2021) 113–118.
[5] Z. Zhang, P. Zhu, C. Li, et al., Chin. Chem. Lett. 32 (2021) 154–157.
[6] X. Cui, J. Chen, Z. Sun, et al., Adv. Funct. Mater. 33 (2023) 2212100.
[7] Q. Huang, M. Wang, L. Zhang, et al., Energy Storage Mater. 45 (2022) 389–398.
[8] J.M. Lee, G. Singh, W. Cha, et al., ACS Energy Lett. 5 (2020) 1939–1966.
[9] T. Wang, D. Legut, Y. Fan, et al., Nano Lett. 20 (2020) 6199–6205.
[10] Y. Liu, C. Yang, Q. Zhang, et al., Energy Storage Mater. 22 (2019) 66–95.
[11] J. Dewulf, G. Van Der Vorst, K. Denturck, et al., Resour. Conserv. Recycl. 54 (2010) 229–234.
[12] Q. Pan, Z. Tong, Y. Su, et al., Adv. Funct. Mater. 31 (2021) 2103912.
[13] X. Liu, T. Ji, H. Guo, et al., Electrochem. Energy Rev. 5 (2022) 401–433.
[14] N. Zhang, X. Li, T. Hou, et al., Chin. Chem. Lett. 31 (2020) 1221–1225.
[15] F. Xie, Z. Xu, A.C. Jensen, et al., Adv. Funct. Mater. 29 (2019) 1901072.
[16] C. Xu, A.R. Puente-Santiago, D. Rodríguez-Padrón, et al., Chem. Soc. Rev. 50 (2021) 4856–4871.
[17] Y. Dai, C. Wang, C. Zhang, et al., J. Alloys Compd. 805 (2019) 631–637.
[18] X. Zhang, H. Shi, L. Liu, et al., J. Colloid Interface Sci. 605 (2022) 472–482.
[19] V.V. Mitic, G. Lazovic, D. Mirjanic, et al., Mod. Phys. Lett. B 34 (2020) 2050421.
[20] B.B. Mandelbrot, Mod. Phys. Lett. B 72 (1975) 3825–3828.
[21] F. Gaboriaud, D. Chaumont, A. Nonat, et al., J. Appl. Crystallogr. 33 (2000) 597–599.
[22] R. Lu, S. Zhou, S.M. Chai, et al., J. Phys. D: Appl. Phys. 55 (2022) 334001.
[23] R. Diduszko, A. Swiatkowski, B. Trznadel, Carbon 38 (2000) 1153–1162.
[24] Q. Lv, Z. Li, L.Z. Liu, et al., Philos. Mag. Lett. 101 (2021) 60–67.
[25] Y. Liu, M. Paskevicius, M.V. Sofianos, et al., Carbon 172 (2021) 454–462.
[26] P. Tancredi, O.M. Londono, P.C.R. Rojas, et al., Mater. Res. Bull. 107 (2018) 255–263.
[27] L. Zhu, X.X. Yang, Y.H. Xiang, et al., Rare Met. 40 (2021) 1383–1390.
[28] B. Yin, S. Liang, D. Yu, et al., Adv. Mater. 33 (2021) 2100808.
[29] P. Yu, W. Tang, F.F. Wu, et al., Rare Met. 39 (2020) 1019–1033.
[30] C.X. Yu, Y. Li, Z.H. Wang, et al., Rare Met. 41 (2022) 1616–1625.
[31] N.T. Aristote, K. Zou, A. Di, et al., Chin. Chem. Lett. 33 (2022) 730–742.
[32] Y. Wan, K. Song, W. Chen, et al., Angew. Chem., Int. Ed. 133 (2021) 11582–11587.
[33] J. Chen, X. Fan, Q. Li, et al., Nat. Energy 5 (2020) 386–397.
[34] H.A. Abubshait, T. Alhashim, H.H. Flemban, et al., Int. J. Energy Res. 45 (2020) 5283–5292.
[35] X. Lian, N. Xu, Y. Ma, et al., Chem. Eng. J. 421 (2021) 127755.
[36] T. Hou, B. Liu, X. Sun, et al., ACS Nano 15 (2021) 6735–6746.
[37] S. Tao, W. Huang, H. Xie, et al., RSC Adv. 7 (2017) 39427–39433.
[38] L. Zhou, K. Zhang, J. Sheng, et al., Nano Energy 35 (2017) 281–289.